

University of California
Los Angeles

Numerical Studies of Turbulence in LAPD

A dissertation submitted in partial satisfaction
of the requirements for the degree
Doctor of Philosophy in Physics

by

Brett Cory Friedman

2013

© Copyright by
Brett Cory Friedman
2013

Abstract of the Dissertation

Numerical Studies of Turbulence in LAPD

by

Brett Cory Friedman

Doctor of Philosophy in Physics

University of California, Los Angeles, 2013

Professor Troy A. Carter, Chair

To be completed

The dissertation of Brett Cory Friedman is approved.

Warren B. Mori

George J. Morales

Russel E. Caflisch

Troy A. Carter, Committee Chair

University of California, Los Angeles

2013

To be completed . . .

TABLE OF CONTENTS

1	Introduction	1
2	Turbulence and Instability	2
2.1	The Kolmogorov Paradigm of Turbulence	2
2.2	The Standard Plasma Paradigm of Linear Instability	2
2.3	Nonlinear Stability Effects	2
2.4	Nonlinear Stability Effects in Plasma Physics	2
3	The Braginskii Fluid Model and LAPD	3
3.1	LAPD Suitability to the Braginskii Fluid Model	3
3.2	The Braginskii Equations	5
3.3	The Vorticity Equation	7
3.4	Minimizing the Equation Set for LAPD Parameters	9
3.4.1	The Reduced Equations	9
3.4.2	The Electrostatic Justification	10
4	LAPD Simulation Details	15
4.1	The Equations	15
4.1.1	Sources	17
4.1.2	Artificial Diffusion and Viscosity	20
4.2	Boundary Conditions	22
4.2.1	Simple Boundaries	23
4.2.2	Bohm Sheath Boundaries	23
4.3	Profiles and Parameters	26

5	The Nature of LAPD Turbulence	30
5.1	LAPD Linear Instabilities	31
5.1.1	Drift Waves	31
5.1.2	Conducting Wall Mode	34
5.2	LAPD Turbulence: A Visual Examination	36
5.3	LAPD Turbulence: A Statistical Examination	40
6	Energy Dynamics Formalism	47
6.1	Total Energy and Dynamics	47
6.2	Spectral Energy Dynamics	47
7	Nonlinear Instability for the Periodic Simulation	48
7.1	The Energy Spectra	48
7.2	Energy Dynamics Result	48
7.3	$n=0$ Suppression	48
8	Energy Dynamics for the Non-periodic Simulations	49
8.1	The Importance of Axial Boundary Conditions	49
8.2	Fourier Decomposing Non-periodic Functions	49
8.3	Energy Dynamics Results	49
8.4	Linear vs Nonlinear Structure Correlation	49
9	Finite Mean Flow Simulations	50
9.1	The LAPD Biasing Experiment	50
9.2	New Linear Instabilities	50
9.3	Statistical Comparisons to Experiment	50

9.4	Energy Dynamics Results	50
10	Conclusion	51
A	The BOUT++ Code	52
A.1	The Object-Oriented Fluid Framework	52
A.2	Explicit Finite Differences	52
A.3	The Physics Inputs	52
B	Grid Convergence	53
	References	54

LIST OF FIGURES

3.1	Electromagnetic statistics comparison	14
4.1	a) Profile relaxation and b) evolved density source	19
4.2	Equilibrium density and electron temperature profiles	26
5.1	Linear drift wave a) growth rates and b) axial structures	33
5.2	Linear conducting wall mode a) growth rates and b) axial structures	35
5.3	3D turbulent simulation animation	37
5.4	RMS time evolution of a) fluctuations and b) axial mode numbers	39
5.5	Turbulent movies	40
5.6	Density statistics	45
5.7	Potential statistics	46

LIST OF TABLES

4.1	LAPD simulation parameters	29
-----	--------------------------------------	----

Acknowledgments

To be completed . . .

Vita

2003-2007	Regent Scholar, University of California, Irvine.
2007	B.S. (Physics) Summa Cum Laude, University of California, Irvine.
2007	Chancellor's Fellow, University of California, Los Angeles.
2007-2009	Teaching Assistant, Department of Physics and Astronomy, University of California, Los Angeles.
2009-2013	Research Assistant, Department of Physics and Astronomy, University of California, Los Angeles.
2009-2012	ORISE FES Fellow, University of California, Los Angeles.
2012-2013	Dissertation Year Fellow, University of California, Los Angeles.

PUBLICATIONS

B. Friedman, T. A. Carter, M. V. Umansky, D. Schaffner, and B. Dudson, Energy dynamics in a simulation of LAPD turbulence, Phys. Plasmas 19, 102307 (2012).

D. A. Schaffner, T. A. Carter, G. D. Rossi, D. S. Guice, J. E. Maggs, S. Vincena, and B. Friedman, Modification of Turbulent Transport with Continuous Variation of Flow Shear in the Large Plasma Device, Phys. Rev. Lett. 109, 135002 (2012).

S. Zhou, W. W. Heidbrink, H. Boehmer, R. McWilliams, T. A. Carter, S. Vincena, B. Friedman, and D. Schaffner, Sheared-flow induced confinement transition in a linear magnetized plasma, *Phys. Plasmas* 19, 012116 (2012).

B. Friedman, M. V. Umansky, and T. A. Carter, Grid convergence study in a simulation of LAPD turbulence, *Contrib. Plasma Phys.* 52, 412 (2012).

M. V. Umansky, P. Popovich, T. A. Carter, B. Friedman, and W. M. Nevins, Numerical simulation and analysis of plasma turbulence the Large Plasma Device, *Phys. Plasmas* 18, 055709 (2011).

P. Popovich, M.V. Umansky, T.A. Carter, and B. Friedman, Modeling plasma turbulence and transport in the Large Plasma Device, *Phys. Plasmas* 17, 122312 (2010).

P. Popovich, M.V. Umansky, T.A. Carter, and B. Friedman, Analysis of plasma instabilities and verification of the BOUT code for the Large Plasma Device, *Phys. Plasmas* 17, 102107 (2010).

S. Zhou, W. W. Heidbrink, H. Boehmer, R. McWilliams, T. A. Carter, S. Vincena, S. K. P. Tripathi, P. Popovich, B. Friedman, and F. Jenko, Turbulent transport of fast ions in the Large Plasma Device, *Phys. Plasmas* 17, 092103 (2010).

CHAPTER 1

Introduction

CHAPTER 2

Turbulence and Instability

2.1 The Kolmogorov Paradigm of Turbulence

2.2 The Standard Plasma Paradigm of Linear Instability

2.3 Nonlinear Stability Effects

2.4 Nonlinear Stability Effects in Plasma Physics

CHAPTER 3

The Braginskii Fluid Model and LAPD

3.1 LAPD Suitability to the Braginskii Fluid Model

At a basic level, the state of a plasma is described by seven-dimensional distribution functions $f_j(\mathbf{x}, \mathbf{v}, t)$ for each species j . The behavior of the plasma is described by the system of kinetic equations (Boltzmann equations), which evolve the distribution functions forward in time:

$$\frac{\partial f_j}{\partial t} + \mathbf{v} \cdot \nabla f_j + \frac{e_j}{m_j} (\mathbf{E} + \mathbf{v} \times \mathbf{B}) \cdot \frac{\partial f_j}{\partial \mathbf{v}} = \left(\frac{\partial f_j}{\partial t} \right)_C. \quad (3.1)$$

$\left(\frac{\partial f_j}{\partial t} \right)_C$ is the change in the distribution function due to collisions. For plasmas, the collisions are Coulomb collisions, and the collision term takes the form of the Fokker-Planck operator. With this operator, Eq. 3.1 is called the Fokker-Planck equation. Now it is well known that the Fokker-Planck equation cannot be solved numerically for problems that require time intervals much larger than the electron-cyclotron time due to computational and time limitations. The phase space is just too large. Therefore, reduced equations, such as gyrokinetic, drift kinetic, or fluid equations have been derived to produce numerically tractable equations. These equations are all derived under certain physical assumptions such as strong guiding magnetic fields, small fluctuation levels, or slow spatial and/or time variations such that these different equations are best applied to different physical situations.

The equations that are arguably most suitable to describe waves and turbulence in LAPD (and fastest to solve numerically) are the fluid equations, specif-

ically those derived by Braginskii [Bra65]. In deriving his equations, Braginskii approximates the solution as $f_j = f_j^0 + f_j^1$ where the zero-order piece f_j^0 is a Maxwellian and the first-order piece f_j^1 is a perturbation on the zero-order distribution function: $|f_j^1| \ll f_j^0$. The equations are then derived by taking moments of the Fokker-Planck equation to create coupled equations of the independent variables, n_j , \mathbf{v}_j , and T_j . Now certain requirements must hold to justify the Braginskii approximation, all of which have the flavor that macroscopic quantities must vary slowly in time and space. This is generally caused by strong relaxation processes such as collisions, which keep the distribution functions close to Maxwellians. In general, for the Braginskii equations to be applicable, processes of interest must occur on time intervals much greater than the collision time and quantities should vary slowly over distances traversed by the particles between collisions.

Specifically, the requirement that time variations must be slow can be written $\frac{d}{dt} \ll \nu$, where for electron drift wave turbulence, this is approximately $\omega_* \ll \nu_e$. Table 4.3, which displays typical LAPD operating parameters, shows that $\omega_*/\nu_e \sim 0.01$. The requirement that spatial quantities vary slowly compared to the collisional mean free path can be written simply for the direction parallel to the magnetic field as $\lambda_{ei} \sim \lambda_{ee} \ll L_{\parallel}$. For LAPD, $\lambda_{ei}/L_{\parallel} \sim 0.01$. For the direction perpendicular to the magnetic field, the same kind of relation $\lambda_{mfp} \ll L_{\perp}$ must also hold. However, due to the cyclotron motion of particles around the magnetic field, λ_{mfp} is really the larmor radius, unless the collisional mean free path is less than the larmor radius. For electrons, $\rho_e \ll \lambda_{ei}$ and $\rho_e/L_{\perp} \sim 10^{-4}$ where $L_{\perp} \sim 0.1$ m. For the ions, the ion cyclotron frequency is close to the ion collision frequency, meaning that either the ion larmor radius or the ion mean free path may be used. Using the larmor radius, $\rho_i/L_{\perp} \sim 0.01$. Therefore, the collisionality is high enough and the machine dimensions are large enough so that the Braginskii fluid model should be applicable to LAPD.

3.2 The Braginskii Equations

The Braginskii fluid equations are as follows: the continuity equation for species j , electrons or ions, is [Wes04, Bra65]

$$\frac{\partial n_j}{\partial t} = -\nabla \cdot (n_j \mathbf{v}_j). \quad (3.2)$$

The momentum balance equation is

$$n_j m_j \frac{d\mathbf{v}_j}{dt} = -\nabla p_j - \frac{\partial \Pi_{j\alpha\beta}}{\partial x_\beta} + n_j e_j (\mathbf{E} + \mathbf{v}_j \times \mathbf{B}) + \mathbf{R}_j. \quad (3.3)$$

$p_j = n_j T_j$ is the pressure. $\Pi_{j\alpha\beta}$ is the stress tensor, which involves the products of viscosity coefficients and rate-of-strain tensor components. The viscosity coefficients are some of the several terms that are called transport coefficients. The transport coefficients are calculated by the Braginskii procedure in terms of n , \mathbf{v} , and T . \mathbf{R}_j , which involves several other transport coefficients, is the rate of collisional momentum transfer. The momentum transfer from ions to electrons is given by

$$\mathbf{R}_e = -m_e n_e \nu_e (0.51 u_{\parallel e} + \mathbf{u}_{\perp e}) - 0.71 n_e \nabla_{\parallel} T_e - \frac{3}{2} \frac{n_e \nu_e}{\omega_{ce}} \mathbf{b} \times \nabla T_e \quad (3.4)$$

where $\mathbf{u} = \mathbf{v}_e - \mathbf{v}_i$ and ν_e is the electron collision frequency with ions. \mathbf{R}_e includes both the friction force and the thermal force, which, like the friction force, is due to electron-ion collisions, but originates from the temperature dependence of the collisionality. The thermal force terms are those proportional to the gradients of temperature. $\mathbf{R}_i = -\mathbf{R}_e$ in a fully ionized plasma with one ion species. However, LAPD has a significant neutral density. Collisions with neutrals are much more important for the ions [PUC10a]. So

$$\mathbf{R}_i = -\mathbf{R}_e - n_i m_i \nu_{in} \mathbf{v}_i. \quad (3.5)$$

The energy balance equation is

$$\frac{3}{2}n_j\frac{\partial T_j}{\partial t} = -n\mathbf{v}_j \cdot \nabla T_j - p_j \nabla \cdot \mathbf{v}_j - \nabla \cdot \mathbf{q}_j - \Pi_{j\alpha\beta} \frac{\partial v_{j\alpha}}{\partial x_\beta} + Q_j \quad (3.6)$$

where the term involving the stress tensor describes viscous heating. The electron heat flux (with more transport coefficients) is

$$q_e = n_e T_e \left(0.71 u_{\parallel} + \frac{3\nu_e}{2\omega_{ce}} \mathbf{b} \times \mathbf{u} \right) + \frac{n_e T_e}{m_e \nu_e} \left(-3.16 \nabla_{\parallel} T_e - \frac{4.66 \nu_e^2}{\omega_{ce}^2} \nabla_{\perp} T_e - \frac{5\nu_e}{2\omega_{ce}} \mathbf{b} \times \nabla T_e \right) \quad (3.7)$$

where the first part of this expression constitutes convection, while the second part is conduction. The ion heat flux is

$$q_i = \frac{n_i T_i}{m_i \nu_i} \left(-3.9 \nabla_{\parallel} T_i - \frac{2\nu_i^2}{\omega_{ci}^2} \nabla_{\perp} T_i - \frac{5\nu_i}{2\omega_{ci}} \mathbf{b} \times \nabla T_i \right). \quad (3.8)$$

The last transport coefficients are in the heating Q . The ion heating due to collisional heat exchange between ions and electrons is

$$Q_i = \frac{3m_e}{m_i} n_e \nu_e (T_e - T_i) \quad (3.9)$$

while the electron heating is

$$Q_e = -\mathbf{R} \cdot \mathbf{u} - Q_i. \quad (3.10)$$

The electron heat exchange involves an ohmic heating contribution ($\mathbf{R} \cdot \mathbf{u}$) that is absent from the ion heating because electrons colliding with ions transfer very little momentum to the ions.

3.3 The Vorticity Equation

Now the Braginskii equations in the previous section contain electric and magnetic fields which must be self-consistently determined by the charges and currents that are evolved by the equations. This is done with the inclusion of Maxwell's equations. Two of those equations are used to write the fields in terms of potentials:

$$\begin{aligned}\mathbf{E} &= -\nabla\phi - \frac{\partial\mathbf{A}}{\partial t} \\ \mathbf{B} &= \nabla \times \mathbf{A}.\end{aligned}\tag{3.11}$$

The vector potential \mathbf{A} is strictly a fluctuating quantity, meaning it is not used to describe the guide field \mathbf{B}_0 . The next equation,

$$\nabla \times \mathbf{B} = \nabla(\nabla \cdot \mathbf{A}) - \nabla^2 \mathbf{A} = \mu_0 \mathbf{j}\tag{3.12}$$

is used to relate the vector potential to the current, where the displacement current is neglected as is generally done in plasmas. The Poisson equation is not that useful for the main part of the plasma, in which the quasineutrality relation, $n_e = n_i \equiv n$, holds. The useful equation that can be used instead is the conservation of charge (or ambipolarity condition), $\nabla \cdot \mathbf{j} = 0$. The vorticity equation is derived from this conservation of charge equation.

The current is $\mathbf{j} = en(v_{\parallel i} - v_{\parallel e}) + en(\mathbf{v}_{\perp i} - \mathbf{v}_{\perp e})$. In LAPD, the parallel current is carried primarily by the fast streaming electrons, while the perpendicular current is primarily carried by the ions, which have larger Larmor radii. So the conservation of charge equation can be simplified to

$$\nabla_{\parallel}(nv_{\parallel e}) = \nabla_{\perp} \cdot (n\mathbf{v}_{\perp i}).\tag{3.13}$$

The perpendicular ion component of this equation is derived from Eq. 3.3

for the ions. Neglecting terms that have finite ion temperature (pressure and stress tensor), and solving for the ion velocity in the Lorentz force term, the perpendicular ion velocity has three terms [PUC10a, SC03]:

$$\mathbf{v}_{\perp i} = \mathbf{v}_E + \mathbf{v}_{pi} + \mathbf{v}_{\nu i} \quad (3.14)$$

where the $\mathbf{E} \times \mathbf{B}$ velocity is $\mathbf{v}_E = \mathbf{E} \times \mathbf{B} / B^2 = -\nabla_{\perp} \phi \times \mathbf{B} / B^2$, the polarization velocity is $\mathbf{v}_{pi} = (1/\omega_{ci}) \mathbf{b} \times (\partial_t + \mathbf{v}_i \cdot \nabla) \mathbf{v}_i$, and the Pedersen velocity is $\mathbf{v}_{\nu i} = (\nu_{in}/\omega_{ci}) \mathbf{b} \times \mathbf{v}_i$. The charge conservation equation then takes the form:

$$\nabla_{\parallel} (nv_{\parallel e}) = \frac{1}{\omega_{ci}} \nabla_{\perp} \cdot [n \mathbf{b} \times (\partial_t + \mathbf{v}_i \cdot \nabla + \nu_{in}) \mathbf{v}_i]. \quad (3.15)$$

Note that the $\mathbf{E} \times \mathbf{B}$ velocity doesn't contribute to the current due to the electrons producing an equal and opposite $\mathbf{E} \times \mathbf{B}$ current. I now employ the approximation $\mathbf{v}_i \sim \mathbf{v}_E$ to Eq. 3.15. This approximation wasn't appropriate of course for Eq. 3.14 due to the fact that \mathbf{v}_E doesn't contribute to the current, but it is appropriate here. Then,

$$\begin{aligned} \nabla_{\parallel} (nv_{\parallel e}) &= \frac{1}{\omega_{ci}} \nabla_{\perp} \cdot [n \mathbf{b} \times (\partial_t + \mathbf{v}_E \cdot \nabla + \nu_{in}) \mathbf{v}_E] \rightarrow \\ \nabla_{\parallel} (nv_{\parallel e}) &= -\frac{m_i}{eB^2} \nabla_{\perp} \cdot [n \mathbf{b} \times (\partial_t + \mathbf{v}_E \cdot \nabla + \nu_{in}) \nabla_{\perp} \phi]. \end{aligned} \quad (3.16)$$

Next, defining the vorticity as $\varpi \equiv \nabla_{\perp} \cdot (n \nabla_{\perp} \phi)$, the vorticity equation reads,

$$\frac{\partial \varpi}{\partial t} = -\mathbf{v}_E \cdot \nabla_{\perp} \varpi - \nabla_{\perp} \mathbf{v}_E : \nabla_{\perp} (n \nabla_{\perp} \phi) - \frac{eB^2}{m_i} \nabla_{\parallel} (nv_{\parallel e}) - \nu_{in} \varpi. \quad (3.17)$$

Finally, the term with the tensor product can be rewritten in a different form [PUC10a]:

$$\frac{\partial \varpi}{\partial t} = -\mathbf{v}_E \cdot \nabla_{\perp} \varpi + \frac{1}{2} (\mathbf{b} \times \nabla_{\perp} n) \cdot \nabla_{\perp} \mathbf{v}_E^2 - \frac{eB^2}{m_i} \nabla_{\parallel} (nv_{\parallel e}) - \nu_{in} \varpi. \quad (3.18)$$

3.4 Minimizing the Equation Set for LAPD Parameters

3.4.1 The Reduced Equations

The continuity equations 3.2 for electrons and ions do not have to both be used due to the quasineutrality condition $n_e = n_i \equiv n$. So, if one focuses on the electron continuity equation, then,

$$\frac{\partial n}{\partial t} = -\nabla \cdot (n\mathbf{v}_e). \quad (3.19)$$

Now, $\mathbf{v}_e = \mathbf{v}_{\perp e} + v_{\parallel e}$, where $\mathbf{v}_{\perp e} = \mathbf{v}_E + \mathbf{v}_{de} + \mathbf{v}_{pe}$, with the diamagnetic velocity $\mathbf{v}_{de} = \frac{\mathbf{b} \times \nabla p_e}{en_e B}$, which wasn't included for the ions in Eq. 3.14 due to the neglect of ion pressure. To a good approximation, the electron polarization velocity is smaller than the $\mathbf{E} \times \mathbf{B}$ velocity, so that $\nabla \cdot (n\mathbf{v}_{\perp e}) = \mathbf{v}_E \cdot \nabla n$ [PUC10a, SC03]. So, the continuity equation reads

$$\frac{\partial n}{\partial t} = -\mathbf{v}_E \cdot \nabla n - \nabla_{\parallel} (nv_{\parallel e}). \quad (3.20)$$

Next, the momentum equations (Eq. 3.3), of which there are six (three for electron velocity components and three for ion velocity components) are reduced to two here. The first is the vorticity equation (Eq. 3.18), in which I used the perpendicular momentum equations to derive it. The second is the equation for the parallel electron momentum. I neglect the parallel ion momentum equation since $v_{\parallel e} \gg v_{\parallel i}$ for LAPD. The electron parallel momentum equation is then

$$nm_e \frac{\partial v_{\parallel e}}{\partial t} = -nm_e \mathbf{v}_E \cdot \nabla v_{\parallel e} - \nabla_{\parallel} p_e - enE_{\parallel} - 0.71n\nabla_{\parallel} T_e - 0.51m_e n\nu_e v_{\parallel e}, \quad (3.21)$$

where the viscous terms have been neglected. The conservation of energy equations (Eq. 3.6) are left. Since the ion temperature in LAPD is very low

($T_i \leq 1$ eV), the ion energy equation is neglected. The electron energy equation is [SC03]

$$\begin{aligned} \frac{3}{2}n\frac{\partial T_e}{\partial t} = & -\frac{3}{2}n\mathbf{v}_E \cdot \nabla T_e - p_e \nabla_{\parallel} v_{\parallel e} + 0.71T_e \nabla \cdot (nv_{\parallel e}) \\ & + \nabla_{\parallel} (\kappa_{\parallel e} \nabla_{\parallel} T_e) + 0.51m_e n \nu_e v_{\parallel e}^2 - 3\frac{m_e}{m_i} n \nu_e T_e, \end{aligned} \quad (3.22)$$

where $\kappa_{\parallel e} = 3.16 \frac{nT_e}{m_e \nu_e}$.

3.4.2 The Electrostatic Justification

Plasma currents create magnetic fields in plasmas. Often times, analytic and numerical calculations of plasma waves and turbulence neglect the time dependent magnetic field perturbations, focusing only on the electrostatic contribution to the waves, turbulence, and transport. In the reduced fluid equations of the previous subsection, the magnetic perturbation enters in two important ways. First, it enters the electric field term of Eq. 3.21 because $E_{\parallel} = -\nabla_{\parallel} \phi - \frac{\partial A_{\parallel}}{\partial t}$, where A_{\parallel} is the parallel component of the vector potential. Second, it affects the parallel gradient operator, $\nabla_{\parallel} = \mathbf{b} \cdot \nabla$ where \mathbf{b} is in the direction of the total magnetic field [SC03]. In the electrostatic limit, $A_{\parallel} \rightarrow 0$, so $E_{\parallel} = -\nabla_{\parallel} \phi$ and $\nabla_{\parallel} = \mathbf{b}_0 \cdot \nabla$. I take this limit in the remaining chapters, but there is the question of how justified I am to do so.

As a first step in answering this question, examine Eq. 3.21. The four independent variables, $n, \phi, v_{\parallel e}$, and T_e , which each have their own evolution equation, are all present in Eq. 3.21. Taking the parallel projection of Eq. 3.12 gives

$$\nabla_{\perp}^2 A_{\parallel} = -\mu_0 j_{\parallel} = \mu_0 n e v_{\parallel e}. \quad (3.23)$$

So $A_{\parallel} \sim \mu_0 n e L_{\perp}^2 v_{\parallel e}$, where $\nabla_{\perp}^2 \sim 1/L_{\perp}^2$. Then, Eq. 3.21 can be approximately rewritten as,

$$nm_e \frac{dv_{\parallel e}}{dt} \sim -T_e \nabla_{\parallel} n + en \nabla_{\parallel} \phi + \mu_0 e^2 n^2 L_{\perp}^2 \frac{\partial v_{\parallel e}}{\partial t} - 1.71 n \nabla_{\parallel} T_e - 0.51 m_e n \nu_e v_{\parallel e}. \quad (3.24)$$

The electromagnetic induction term, ($EM = en \frac{\partial A_{\parallel}}{\partial t}$) is now written in terms of $v_{\parallel e}$ as $EM = \mu_0 e^2 n^2 L_{\perp}^2 \frac{\partial v_{\parallel e}}{\partial t}$. It can therefore be directly compared to the other terms proportional to $v_{\parallel e}$ to test for its importance. The other terms are the inertial term, $M = nm_e \frac{dv_{\parallel e}}{dt}$ and the resistive term, $R = 0.51 m_e n \nu_e v_{\parallel e}$. A common way to compare these terms is to approximate the time derivative as the ion cyclotron frequency $\frac{\partial}{\partial t} \sim \omega_{ci}$ and the perpendicular length scale as the ion sound gyroradius $L_{\perp} \sim \rho_s$, where $\rho_s = c_s / \omega_{ci}$. Then the ratio of the three terms (obtained by dividing each term by $eBnv_{\parallel e}$) is:

$$M : EM : R = \frac{m_e}{m_i} : \beta : \frac{0.51 \nu_e}{\omega_{ce}}. \quad (3.25)$$

It can be seen from Table 4.3 that in LAPD, this ratio is 1 : 3.6 : 1.5. Thus, all three terms are of the same order with the electromagnetic term slightly larger than the other two. It seems then quite unjustified to use an electrostatic approximation.

However, estimating $\frac{\partial}{\partial t} \sim \omega_{ci}$ isn't necessarily accurate. The equation set describes drift waves and so a more proper estimate might be $\frac{\partial}{\partial t} \sim \omega_*$. Under this approximations, the ratio is 1 : 3.6 : 70, meaning that the resistive term is more than an order of magnitude larger than the other two; however, the approximation $\frac{\partial}{\partial t} \sim \omega_*$ is still rough and the numerical value of ω_* in Table 4.3 is somewhat of a rough itself. Moreover, one could also argue with the approximation of the perpendicular length scale as the sound gyroradius. This is probably too small, in which case the electromagnetic inductance has been underestimated. While it's clear that the inertial term is probably unimportant, the inductive term could be important.

Similarly, the contribution of $\tilde{\mathbf{b}} \sim A_{\parallel}$ in ∇_{\parallel} can be approximated in a similar manner with similar inconclusive results. Without a clear separation between the resistive and inductive terms, the best way to determine the validity of the electrostatic approximation is by direct numerical calculation of the turbulence with and without the electromagnetic contributions. Therefore, I simulated an electrostatic and two electromagnetic versions of LAPD turbulence. The details of the electrostatic code are described in Chapter 4 and in Appendix A.

The only difference between the electrostatic and the first electromagnetic simulation is the exclusion/inclusion of the electromagnetic term $en \frac{\partial A_{\parallel}}{\partial t}$ in the parallel electron momentum equation (Eq. 3.21). Of course the Maxwell equation (Eq. 3.12) must also be included for the electromagnetic simulation. The second electromagnetic simulation includes not only this term but also the A_{\parallel} contribution to ∇_{\parallel} in the parallel electron momentum equation.

Now, turbulence is best characterized and compared in a statistical and often spectral manner. More details of turbulence characterization and comparison will be discussed later, but for now, I make a few statistical comparisons between the electrostatic and electromagnetic simulation results. Figure 3.1 shows the results of the three simulations as well as the experiment – namely, a comparison of the frequency spectra, the probability distribution function (pdf), and the rms level of the density fluctuations. The “Full Electromagnetic” curves are from the simulation including the A_{\parallel} contribution to ∇_{\parallel} , while the “Electromagnetic” curves just include the A_{\parallel} contribution to E_{\parallel} . Clearly, the fluctuations are statistically similar in all cases and none of the simulations are inconsistent with the experiment. However, the electromagnetic effects are noticable, and as I include more electromagnetic contributions in the simulations, the turbulent statistics more closely resemble those of the experiment. I make no quantitative comparison here, but rely only on a visual examination in making this conclusion.

Now, as mentioned above, I do not include any electromagnetic contributions

in the simulations used in the following chapters. It seems rather unjustified to do so since I am clearly able to run electromagnetic simulations and they seem to reproduce experimental turbulence with slightly better accuracy than the electrostatic ones. One justification for my abandonment of electromagnetic simulations, however, is that electromagnetic simulations take a bit longer than electrostatic ones due to the extra relation in Eq. 3.12 that is used to solve for A_{\parallel} , which requires an inversion of the Laplacian. This takes extra computation. Another justification is that the electromagnetic equations make the energy dynamics analysis in Chapter 6 a bit more complicated. Both of these factors are mitigated, however, if the inertial term $nm_e \frac{dv_{\parallel e}}{dt}$ is dropped. Nevertheless, at the beginning of this work, I strived to find the simplest possible model to describe the turbulence in LAPD, and I determined that the electrostatic approximation was acceptable. At that time, I didn't have the results of Fig. 3.1. If I had the time, I would redo all of the simulations and analysis to include electromagnetic contributions, but drop the inertial term in Eq. 3.21. This is a clear route to take for future work. Nevertheless, I am confident that electromagnetics would not change any of my conclusions in this work. So for the remainder of this work, I will present theoretical calculations, simulation results, and conclusions using the electrostatic approximation.

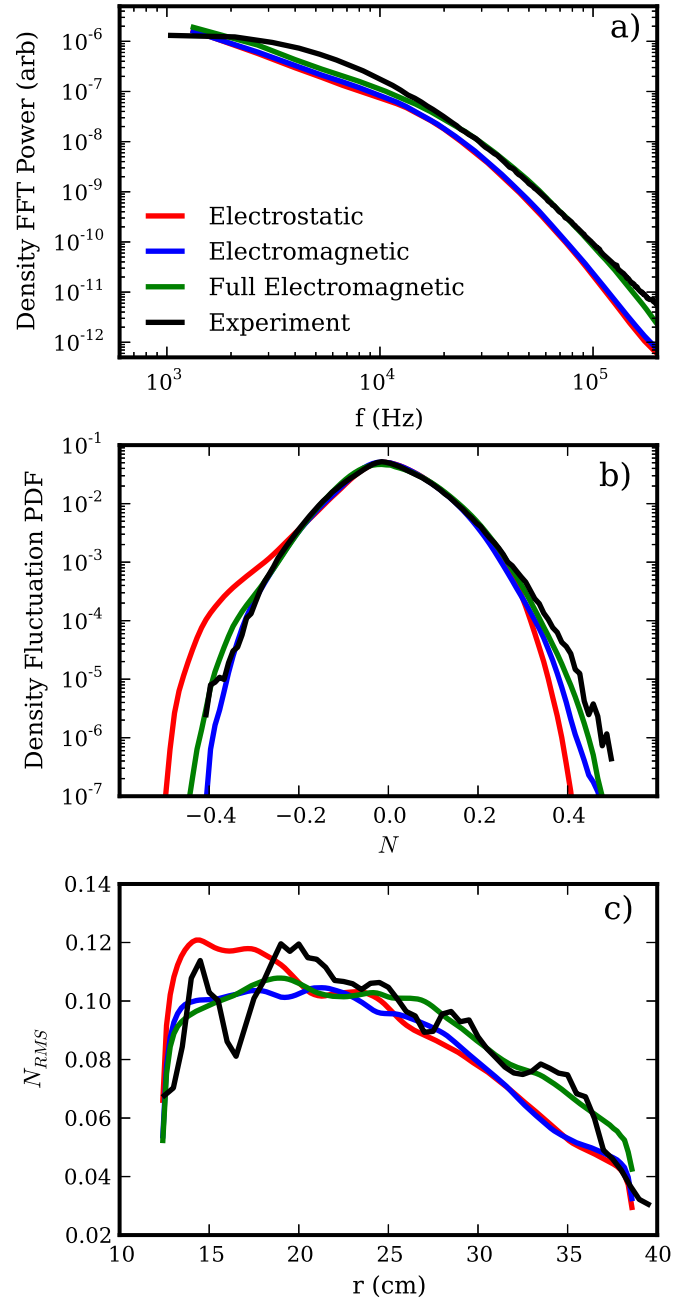


Figure 3.1: Electromagnetic statistics comparison

CHAPTER 4

LAPD Simulation Details

In this chapter, I state and explain the equations, boundary conditions, parameters, and profiles that I use in the LAPD simulations. There are two main classes of simulations: those with a mean radial electric field and those without. The simulations with the mean radial electric field will be explored in Chapter 9. This chapter and all those up to Chapter 9 deal with the simulations with no mean radial electric field. There are only four different simulations that are used until Chapter 9, and they differ in only one way: their axial boundary conditions, which are explained in Sec. 4.2.

I solve the equations using the BOUT++ code [DUX09]. The code is discussed and partially displayed in Appendix A, and specific numerical routines and other details are described there as well.

4.1 The Equations

I use the Braginskii equations as shown in Chapter 3 to model LAPD turbulence. I separate all variables into time-independent equilibrium parts and time-dependent fluctuating parts. I do this in order to input experimental time-independent profiles. The alternative would be to solve the full equations with no equilibrium/fluctuation separation and no experimental profile input. The difficulty in this alternative technique is the need to specify sources, sinks, and boundary conditions, which can be difficult to measure or estimate. This alternative method has

been undertaken by Rogers and Ricci [RR10]. Our approach is easier, and since the time-independent profiles are so important in driving the turbulence, I feel that inputting the experimentally measured profiles can help produce physically realistic turbulence.

Now due to the equilibrium/fluctuation separation technique, I can linearize the equations, keeping only one nonlinearity in each equation: the advective nonlinearity. While this isn't necessary, it does simplify the energy dynamics as formulated in Chapter 6. The justification is practical rather than mathematical, and the partially linearized equations produce fluctuations that are quite statistically similar to experimental fluctuations, which is shown in Chapter 5, so I feel justified in doing this.

In the equations below, I normalize all quantities to give dimensionless variables. All times are normalized to the inverse ion cyclotron frequency $\omega_{ci} = \frac{eB}{m_i}$, velocities are normalized to the ion sound speed $c_s = \sqrt{\frac{T_e}{m_i}}$, lengths are normalized to the sound gyro-radius $\rho_s = c_s/\omega_{ci}$, potentials to T_e/e , densities to the density at the radial cylindrical axis, and temperatures to the temperature at the cylindrical axis. Quantities such as c_s that are typically functions of radius due to the radial dependence of the electron temperature are taken to be constant in these normalizations, where I use the values at the radial axis. The equations below don't reflect this, but the transport coefficients in the actual code do. So, the LAPD simulation equations are as follows:

$$\partial_t N = -\mathbf{v}_E \cdot \nabla N_0 - N_0 \nabla_{\parallel} v_{\parallel e} + \mu_N \nabla_{\perp}^2 N + S_N + \{\phi, N\}, \quad (4.1)$$

$$\partial_t v_{\parallel e} = -\frac{m_i}{m_e} \frac{T_{e0}}{N_0} \nabla_{\parallel} N - 1.71 \frac{m_i}{m_e} \nabla_{\parallel} T_e + \frac{m_i}{m_e} \nabla_{\parallel} \phi - \nu_e v_{\parallel e} + \{\phi, v_{\parallel e}\}, \quad (4.2)$$

$$\partial_t \varpi = -N_0 \nabla_{\parallel} v_{\parallel e} - \nu_{in} \varpi + \mu_{\phi} \nabla_{\perp}^2 \varpi + \{\phi, \varpi\}, \quad (4.3)$$

$$\begin{aligned} \partial_t T_e = & -\mathbf{v}_E \cdot \nabla T_{e0} - 1.71 \frac{2}{3} T_{e0} \nabla_{\parallel} v_{\parallel e} + \frac{2}{3 N_0} \kappa_{\parallel e} \nabla_{\parallel}^2 T_e \\ & - \frac{2 m_e}{m_i} \nu_e T_e + \mu_T \nabla_{\perp}^2 T_e + S_T + \{\phi, T_e\}. \end{aligned} \quad (4.4)$$

Note that the advective nonlinearities in each equation are written with Poisson brackets. Additionally, the only equilibrium profiles are N_0 and T_{e0} , which are only functions of radius. $\phi_0 = v_{\parallel e0} = 0$ in these equations. The linearized vorticity is $\varpi = \nabla_{\perp} \cdot (N_0 \nabla_{\perp} \phi)$. N , $v_{\parallel e}$, ϕ , and T_e are fluctuating first-order quantities.

These equations have a few additional terms not included in the equations of Chapter 3. First, I have included density and temperature sources S_N and S_T . I have left out a momentum source as well as the contribution of the density source to changes of the momentum and temperature. Second, I have included diffusive ($\mu_N \nabla_{\perp}^2 N$ and $\mu_T \nabla_{\perp}^2 T_e$) and viscous ($\mu_{\phi} \nabla_{\perp}^2 \varpi$) terms in Eqs. 4.1, 4.4, and 4.3 respectively.

4.1.1 Sources

The density source is actually a source/sink. It models both the ionization of neutral atoms as well as the recombination of ions and electrons. The sink action in LAPD is dominated by parallel (along \mathbf{B}) losses to materials at the machine ends because the magnetic field prevents rapid radial loss. It's also possible that a layer of neutral atoms near the end of the machine opposite the cathode cools the plasma enough so that recombination can be strong in this layer. The sink action occurs at all radii with finite plasma density, which constitutes regions both inside and outside of the cathode radius due to radial ion transport. If the sink action is primarily at the end plates, the sink can be calculated by $2n_{se}c_s/L_{\parallel}$, where n_{se} is the density at the sheath edge in front of the end plate, c_s is the sound speed at the sheath edge, and the factor of 2 accounts for the two plates. n_{se} and c_s are functions of radius such that the sink is strongest at the radial axis and decreases at larger radii. Calculation of the sink term requires knowledge of the density and temperature at the end of the machine, which is generally not measured experimentally.

The ionization source occurs primarily inside of the cathode radius. The source term is calculated with $n_e n_n \langle \sigma v \rangle_{iz}$, where n_n is the neutral Helium density and $\langle \sigma v \rangle_{iz}$ is the ionization rate of Helium and is a strong function of temperature. The strong temperature dependence is the reason why ionization occurs only within the cathode radius. Ionization rates are readily available [Sta00], but the neutral density is not, making the source difficult to calculate. However, it is clear that if one were to sum up the source and sink and integrate axially, the region inside of the cathode radius must be a net source, while the region outside of it must be a net sink.

Now when I simulate the turbulence in LAPD without the source terms, turbulence drives radial transport such that the total flux-surface-averaged density gradient relaxes over time as seen in Fig. 4.1 a) until the radial transport ceases. It's interesting that $\langle N_t \rangle_{fs} = \langle N_0 + N \rangle_{fs}$ doesn't become totally flat, but maintains a gradient. This is probably a result of the partial linearization of the equations, especially the diffusion term $\mu_N \nabla_\perp^2 N$, and possibly boundary conditions. Nevertheless, the strong relaxation is not physical due to the presence of the physical source/sink mechanism. (Note that the equilibrium density profile N_0 used in the simulation to make Fig. 4.1 a) is not the same N_0 shown in Fig. 4.2. I show the relaxation of the profile in Fig. 4.1 a) because it has a very steep gradient, which makes the relaxation effect more pronounced and easier to see.)

Now, rather than developing a first principle's source based on the theoretical source/sink expressions, I use ad hoc controlling sources. I estimate that $\langle N_t \rangle_{fs}$ remains constant over time, and model the source using the integral portion of a PID controller. This means that I write an equation for the source:

$$\partial_t S_n = - \langle N \rangle_{fs}. \quad (4.5)$$

Therefore,

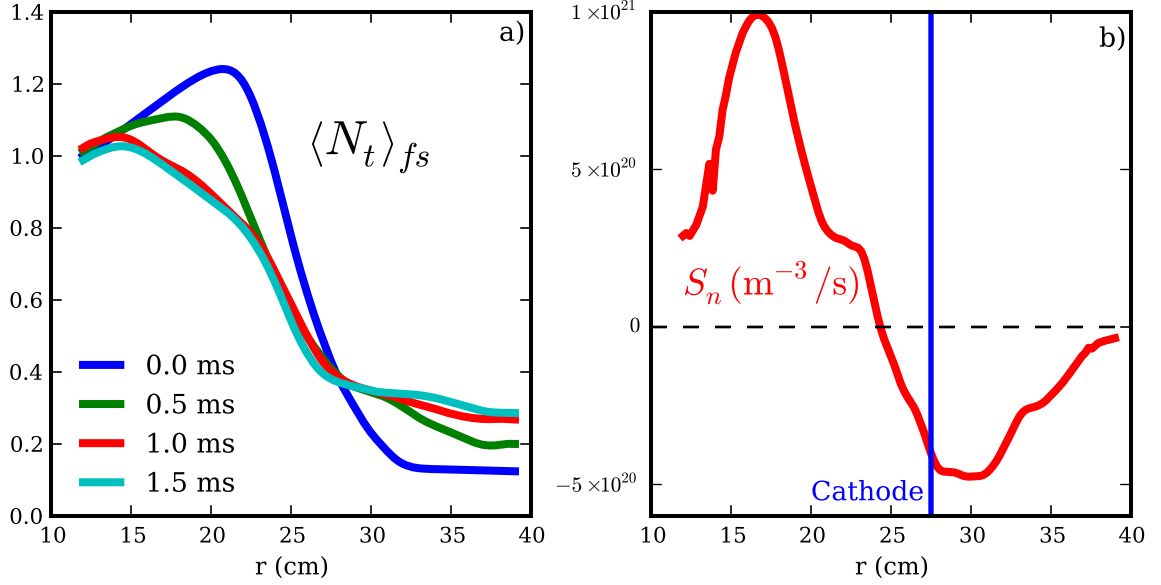


Figure 4.1: a) Profile relaxation and b) evolved density source

$$S_n(t) = - \int_0^t \langle N(\tau) \rangle_{fs} d\tau. \quad (4.6)$$

A typical time-averaged density source is shown in Fig. 4.1 b). The upshot of using such a source is that $\langle N_t(t) \rangle_{fs} \simeq N_0$. Notice that the source in Fig. 4.1 b) is net positive inside of the cathode radius and negative outside of it, just as one would expect. I use the same method for the temperature source. The temperature source ultimately comes from the hot electrons that are boiled off of the cathode, which transfer their energy to the plasma through ionizing collisions. This heat transfer is mostly to the electrons of the plasma. The temperature sink is caused by collisions with ions and neutrals which line radiate and by heat loss to the sheath and end walls.

I emphasize that the sources are not first principle sources. They are constructed based on the simulated radial transport. The alternative first principle's approach was used by Rogers and Ricci for LAPD [RR10]. They use a stationary

top-hat-like ionization source that models the physical density-producing process in LAPD. Furthermore, they do not separate equilibrium from fluctuations or input equilibrium profiles. Their source feeds the density, which then transports itself until it comes to a quasi-equilibrium state (a sink is also present). This method solves for the full plasma state with very little experimental input. They input the sources and derive the plasma state. On the other hand, I input part of the plasma state and derive the sources. As stated before, our method has the advantage of using experimentally measured profiles. This experimental input allows us to more easily simulate turbulence that resembles that in the experiment, and therefore make conclusions on the fluctuation properties. I do not, however, evolve the equilibrium and gain the knowledge that comes from that.

4.1.2 Artificial Diffusion and Viscosity

Artificial diffusion or hyperdiffusion terms are ubiquitous in fluid simulations. They are generally intended to prevent high frequency or high wavenumber ringing caused by numerical advection schemes at steep interfaces. They can, however, cause unphysical smoothing in systems that are non-diffusive and non-viscous or cause over-smoothing if applied haphazardly. Some numerical advection schemes contain their own diffusion, called numerical diffusion. Other non-advective finite difference schemes also contain numerical diffusion or dispersion.

I use artificial diffusion and viscosity for several reasons. The first is to prevent artificial high-wavenumber oscillations due to the Arakawa advection scheme that I use [Ara66]. Second, it smooths out the solutions, preventing the total density and temperature from becoming negative at any point in space, which is obviously unphysical. Third, I can use it to prevent the need to go to very fine grid spacing at which physical diffusion and viscosity are important. Finally, I can use it to help saturate the turbulence at levels consistent with experiment. These reasons are all somewhat related, and more discussion is left to Appendix B.

Diffusion and viscosity are real effects that are present in the non-reduced Braginskii equations. In Chapter 3, I made the approximation that $\nabla \cdot (n\mathbf{v}_{\perp e}) = \mathbf{v}_E \cdot \nabla n$, which neglected the polarization velocity part of $\mathbf{v}_{\perp e}$. Now the “full polarization velocity” [SC03] (from crossing Eq. 3.3 with \mathbf{b} and neglecting the stress tensor) is

$$\mathbf{v}_{pe} = (1/\omega_{ce}) \left[\frac{d(\mathbf{b} \times \mathbf{v}_{\perp e})}{dt} + \nu_e \mathbf{b} \times \mathbf{v}_{\perp e} - \nu_e \mathbf{b} \times \mathbf{v}_{\perp i} - \frac{3}{2} \frac{\nu_e}{m_e \omega_{ce}} \nabla_{\perp} T_e \right]. \quad (4.7)$$

The part of this that causes collisional diffusive terms is $(\nu_e/\omega_{ce})\mathbf{b} \times \mathbf{v}_{\perp e}$. Now this contains $\mathbf{v}_{\perp e}$ itself, which must be approximated as $\mathbf{v}_{\perp e} = \mathbf{v}_E + \mathbf{v}_{de}$ to allow for closure. Only the diamagnetic drift part will be important for the collisional diffusion, so the part of the polarization velocity that I focus on is $(\nu_e/\omega_{ce})\mathbf{b} \times \mathbf{v}_{de}$. Recall that I want to use this in the continuity equation, so I am interested in the term $\nabla \cdot (n_e v_e) \rightarrow \nabla \cdot (n_e (\nu_e/\omega_{ce})\mathbf{b} \times \mathbf{v}_{de}) = -\nabla \cdot \frac{\nu_e m_e}{e^2 B^2} \nabla_{\perp} p_e$. Now defining $D = \frac{\nu_e m_e T_e}{e^2 B^2}$, I have $\nabla \cdot (n_e v_e) = -\nabla \cdot (D \nabla_{\perp} n) + \text{lots of other terms}$. D is the classical diffusion coefficient, which is about $0.01 \text{m}^2/\text{s}$ for LAPD parameters. One of the terms in $\nabla \cdot (D \nabla_{\perp} n)$ is $D \nabla_{\perp}^2 n$, which has the same form of the artificial diffusion term that I’ve added to Eq. 4.1. Of course, I have neglected many terms of the same order as this term in Eq. 4.1, but this shows that such a classical diffusion term is present in the Braginskii equations.

A similar treatment can be used for the energy conservation equation (Eq. 3.6), using the same procedure as for the continuity equation but with the $p_e \nabla \cdot \mathbf{v}_e$ term in Eq. 3.6. The result is $p_e \nabla \cdot \mathbf{v}_e = D n_e \nabla_{\perp}^2 T_e + \text{lots of other terms}$. This has the same form as the temperature diffusion term in Eq. 4.4.

The viscosity in the vorticity equation comes from the ion stress tensor term $\frac{\partial \Pi_{i\alpha\beta}}{\partial x_{\beta}}$ that I neglected when deriving the vorticity equation because I neglected everything with finite ion temperature. If this was included, a vorticity diffusion term (aka a viscosity) would have been included in the vorticity equation [PUC10b]

as it is in other equation sets like the well-known Hasagawa-Wakatani equations [HW83]. The magnetized Braginskii viscosity coefficient is $\eta_1^i = \frac{3nT_i}{10\omega_{ci}^2\tau_i}$, which is about $2 \times 10^{-8} \text{kg/m} \cdot \text{s}$ for LAPD. Since LAPD's ions are not necessarily magnetized due to the fact that $\omega_{ci}\tau_i \sim 1$, the unmagnetized ion viscosity is $\eta_0^i = 0.96nT_i\tau_i$ [Bra65] which is about $4 \times 10^{-7} \text{kg/m} \cdot \text{s}$.

For the artificial diffusion and viscosity coefficients in Eqs. 4.1-4.4, I use a single value of 1.25×10^{-3} in our normalized units, which is $0.075 \text{m}^2/\text{s}$ in real units. I find that this value produces turbulent fluctuation levels consistent with experimental levels. I use this as a free parameter in this sense. This value is much larger than the real classical diffusion D , but is smaller than $\frac{\eta_1^i}{nm_i} = 1 \text{m}^2/\text{s}$. Nevertheless, I neglected a number of terms in Eqs. 4.1-4.4 such that there isn't justification to use the real diffusion and viscosity in these equations. Artificial diffusion and viscosity terms, however, serve a numerical purpose.

4.2 Boundary Conditions

Boundary conditions are often difficult to determine in plasma devices. While the properties of the boundaries are usually known, the way that the plasma interacts with them can be complex. Plasma boundary physics is one of the main elements of present day fusion research [Sta00]. Often times there is uncertainty in the equations that need to be used in simulations, and once the equations are found, they can be difficult to implement in codes.

The boundary conditions in LAPD are difficult to determine. LAPD contains at one end, a hot emitting cathode behind a biased mesh annode. In front of the annode are biasable azimuthal limiters with radius about equal to the cathode radius, though the limiter radius may be changed. The far end contains a floating mesh plate. The cylinder is conducting and has a radius about 20 cm larger than the cathode radius.

4.2.1 Simple Boundaries

In all simulations, I use an annulus rather than a cylinder. Although the inner radius of the annulus may be arbitrarily small, I take the inner radius to be 12 cm. I take the outer radius to be 39 cm. This is generally the radial extent of our experimental probe measurements. Furthermore, the plasma fluctuations are nearly zero (when normalized to values at the cylindrical axis) outside of this annular region, which is seen in Fig. 3.1 c). Therefore, I set the radial boundaries on all of the fluctuating variables (N , ϕ , $v_{\parallel e}$, and T_e) to zero. It would be nice in the future to take data spanning at least a few more cm and extend the simulation domain accordingly. But for now, the results use such an annular domain.

As for the axial boundaries, I use four different boundary conditions: periodic, zero-value (Dirichlet), zero-derivative (Neumann), and Bohm sheath. The only non-trivial one, Bohm sheath, is derived and described in the following subsection. The others are all trivial to implement and provide a test of the importance of the axial boundary conditions on the nature of the turbulence.

4.2.2 Bohm Sheath Boundaries

Bohm sheath boundary conditions are applicable when a plasma terminates at a conducting plate. I note that this is not necessarily the case in LAPD. The cathode/annode system is obviously much different from a simple floating or biased conducting plate. Furthermore, the mesh wall at the far end is not a solid wall. Moreover, it's not clear if the plasma is even attached to the far end mesh wall or if it becomes detached in the neutrals in front of it, where the plasma cools and recombines before interacting with the wall. In any case, it is still instructive to apply such an idealized boundary condition to LAPD because it is somewhat more realistic than the simpler boundary conditions, and it creates a new linear instability (see Sec. 5.1.2), which can be used to test the robustness of LAPD's

nonlinear instability. Therefore, I proceed with the derivation of the Bohm sheath boundary conditions.

Now, it is known that to good approximation, a plasma bounded by a wall can be divided into two regions: the main plasma and the Debye sheath [Sta00]. The Debye sheath is a small region adjacent to the wall, generally several Debye lengths long. It has a net positive charge ($n_i > n_e$) that shields the negative charge on the wall. The sheath does not completely shield the negative wall, however, and a small electric field penetrates into the main plasma (the ambipolar field), which mostly serves to accelerate the cold ions toward the wall, and slightly retard the electrons before entering the sheath. In the main plasma, the quasi-neutrality relation holds ($n_i = n_e$).

The well-known Bohm criterion along with other considerations restricts the ions to move into the sheath entrance at the sound speed $c_s = \sqrt{T_e/m_i}$. I consider here the case where there is no external biasing; in other words, the end plates are electrically isolated and floating. The wall can be set to an arbitrary potential, say $\phi_w = 0$, while the potential at the sheath entrance is then the positive floating potential ϕ_{sf} . This potential difference across the sheath reflects slow electrons that enter the sheath. The electrons approximately maintain a cutoff Maxwellian velocity distribution throughout the sheath, and at the wall, their velocity is retarded by a Boltzmann factor due to the floating potential. In total, the current to the wall is [BRT91, BCR93, XRD93]

$$J_{\parallel} = \pm en \left[c_s - \frac{(T_e/m_e)^{1/2}}{2\sqrt{\pi}} e^{\left(-\frac{e\phi_{sf}}{T_e}\right)} \right], \quad (4.8)$$

where the \pm indicates that the plasma flux goes into the wall, which is in different directions for the different end plates. Note that there is a factor of $\sqrt{2}$ discrepancy between different reports on the expression used for the thermal velocity, which should have only a minor consequence. In this expression, all

values are total (equilibrium + fluctuations).

Now, this is not only the current to the wall, but also the current going into the sheath edge, since the sheath is too small for there to be appreciable radial current loss or an ionization source within the sheath. All values, in fact, are taken to be those at the sheath edge. Furthermore, since the wall is electrically isolated, the equilibrium current at the wall vanishes. This sets the value for the floating potential to be $\phi_{sf} = \Lambda T_{e0}/e$ with $\Lambda = \ln\left(\frac{1}{2\sqrt{\pi}}\sqrt{\frac{m_i}{m_e}}\right)$. Note that T_{e0} is a function of radius, meaning ϕ_{sf} is also a function of radius. Thus, a radial temperature gradient produces a radial electric field, at least at the sheath edge and likely penetrating axially into the main plasma. It is noted that J_{\parallel} need not vanish on every field line since the end plates are conducting and charges can move around on the plate, however, the vanishing equilibrium current is generally a fair approximation [BCR93].

On the other hand, the fluctuating component of the current is allowed to vary between field lines. The first order fluctuating component is obtained by linearizing Eq. 4.8, giving the result:

$$J_{\parallel} = \pm e N_0 c_{s0} \left[\frac{e\phi}{T_{e0}} - \Lambda \frac{T_e}{T_{e0}} \right], \quad (4.9)$$

where now, J_{\parallel} , ϕ and T_e are fluctuating components, consistent with previous notation. This expression for the current sets the fluctuating axial boundary condition of the plasma and is often called the Bohm Sheath boundary condition. This current condition holds both at the wall and at the sheath entrance. So rather than taking the simulation domain all the way to the wall, simulations often end at the sheath entrance and employ this analytically derived boundary condition to the boundaries of the main plasma. Then one doesn't have to worry about the small spatial scales and the non-quasineutrality of the sheath. The corresponding boundary conditions for the other fluid variables such as the density

and temperature have recently been derived by Loizu et al. [LRH12]. However, I simply take them to have zero-gradient as most others have done, although this isn't wholly inconsistent with Loizu's calculations.

Now while one may set the parallel current (or equivalently $v_{\parallel e}$) at the axial boundaries to the quantity on the right hand side of Eq. 4.9, I don't do that. I use Ohm's Law ($-\nabla_{\parallel}\phi = \eta_{\parallel}J_{\parallel}$) to set the boundary condition for the gradient of ϕ . I do this for practical reasons in the coding. Therefore, the boundary condition used in the code is (in our normalized units):

$$\nabla_{\parallel}\phi = \pm \frac{\nu_e m_e}{m_i} (\phi - \Lambda T_e). \quad (4.10)$$

4.3 Profiles and Parameters

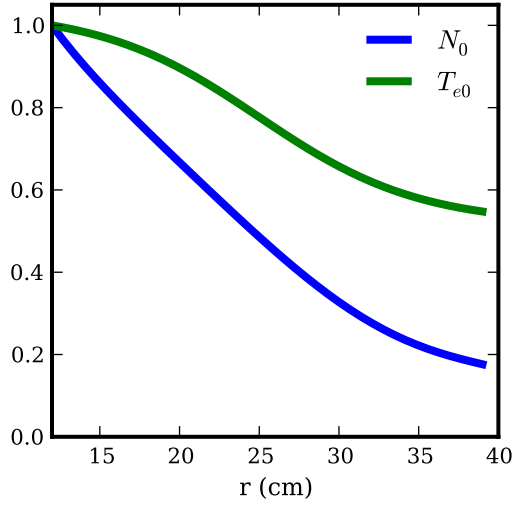


Figure 4.2: Equilibrium density and electron temperature profiles

As explained above, I take all equilibrium profiles and parameters from experimental measurements. All simulations before Chapter 9 use profiles and parameters from one particular experiment. This experiment used limiter biasing to

essentially null out the mean radial electric field [SCR12]. I used this experiment so that I could neglect the mean potential profile in the equations (as is done in Eqs. 4.1-4.4), which simplifies our analysis. The normalized profiles that I use are shown in Fig. 4.2, and the parameters are shown in Table 4.3. The density profile is a polynomial fit to the experimental equilibrium density profile. The temperature profile is a tanh function that somewhat resembles typical LAPD temperature profiles. At the time of the first simulations, I didn't have reliable temperature profile measurements, so I was forced to estimate what the profile might look like. I note that the real temperature profile has a steeper gradient than the one I use. And again, I use $\phi_0 = 0$, which is a good approximation for the experimental nulled out potential profile.

The profiles that I use have no azimuthal or axial variation because I don't have the corresponding experimental measurements. So I assume that the equilibrium profiles are only functions of radius. It's likely, however, that there is some axial variation in the profiles and parameters. In LAPD, $\nu^* \equiv L_{\parallel}/\lambda_{ei} \sim 100$, generally indicating that a parallel temperature gradient can exist depending on the locations of the sources and sinks [Sta00]. Furthermore, if the Bohm sheath boundary condition is correct, the equilibrium potential must have a parallel gradient in order to accelerate the ions up to the sound speed at the sheath entrance. This ambipolar parallel electric field should exist between the location of the sheath entrance and an ion collision length into the main plasma. The parallel electric field generated by the condition of Eq. 4.10 is just the perturbed field that responds to electron temperature perturbations. It doesn't constitute the equilibrium electric field.

Moreover, recall that the Bohm sheath condition combined with a radial equilibrium electron temperature profile implies (at least near the sheath) a corresponding equilibrium potential profile, since $\phi_{sf} = \Lambda T_{e0}/e$. Experimentally, this relation doesn't hold where the plasma is measured, meaning that either the am-

bipolar field doesn't penetrate far into the plasma or that the real LAPD boundary conditions are more complicated than simple floating conducting plates. So I don't use any equilibrium axial variation, leaving this to future work.

Species	${}^4\text{He}$
Z	1
n	$2.86 \times 10^{18} \text{ m}^{-3}$
T_e	6 eV
T_i	$\lesssim 1 \text{ eV}$
B_0	0.1 T
L_{\parallel}	17 m
a	0.4 m
λ_D	10^{-5} m
ω_{ci}	$2.4 \times 10^6 \text{ rad/s}$
ω_{ce}	$1.8 \times 10^{10} \text{ rad/s}$
ρ_e	$5.3 \times 10^{-5} \text{ m}$
ρ_i	$\sim 1 \times 10^{-3} \text{ m}$
ρ_s	$5 \times 10^{-3} \text{ m}$
v_{te}	$9.4 \times 10^5 \text{ m/s}$
c_s	$1.1 \times 10^4 \text{ m/s}$
v_A	$7 \times 10^5 \text{ m/s}$
β	5×10^{-4}
m_e/m_i	1.4×10^{-4}
$\ln\Lambda$	11
ν_e	$7.2 \times 10^6 \text{ Hz}$
λ_{ei}	0.13 m
ν_i	$\sim 10^6 \text{ Hz}$
ν_{in}	$3 \times 10^3 \text{ Hz}$
κ_{\parallel}^e	$9.8 \times 10^{23} \text{ eV/m}^2 \text{ s}$
η_0^i	$\sim 10^{12} \text{ eV s/m}^3$
ω_*	$\sim 5 \times 10^4 \text{ rad/s}$

Table 4.1: LAPD simulation parameters

CHAPTER 5

The Nature of LAPD Turbulence

Simulations can supplement experiment by providing detailed spatial data that is too difficult to obtain experimentally. This spatial data can be analyzed, revealing new properties of the experiment. In order for simulations to provide information, however, they must accurately represent the system which they model. Assessing the validity of simulations generally comes in two parts: verification and validation. Verification, the evidence that the code solves the equations correctly, will not be taken up here. I note, however, that my collaborators and I have done verification studies in the past, somewhat detailed in Popovich et al. [PUC10a]. We compared linear BOUT (the old version of BOUT++) and BOUT++ simulations to analytic solutions as well as to eigensystem solver solutions. On the other hand, I will focus parts of this chapter on our validation effort. Validation is the evidence that the simulation model accurately reproduces features of the experiment. Generally, the more features of the experiment that the model reproduces, the more valid the model. While this chapter focuses on simple analyses to describe the nature of the simulated turbulence, it will also make comparisons, where possible, to experimental data in order to show that the model is relatively well validated. First, however, I analyze the linear instabilities in the LAPD simulations, and this affords no experimental comparison.

5.1 LAPD Linear Instabilities

Linear instabilities are prevalent in plasma physics. They come from the linearization around an equilibrium of the plasma equations. Physically, if a plasma is in a time-independent steady state that is linearly unstable and a finite fluctuation of any size occurs, the fluctuation will grow exponentially. Linear instabilities often drive hydrodynamic and plasma turbulence. I therefore study the linear instabilities of the LAPD system before moving onto the turbulence because they can offer insight into the nature of the turbulence. The LAPD equations, parameters, and profiles described in Chapter 4 give rise to a couple of linear instabilities. They are both drift wave type instabilities, but they have different pressure/potential coupling mechanisms. One type couples through the adiabatic response, while the other couples through the sheath boundary response.

5.1.1 Drift Waves

Electron drift waves driven by an equilibrium density or pressure gradient that use the adiabatic response are generally referred to as just drift waves or the universal instability. The electron drift wave mechanism is the following: An electron pressure fluctuation in the plasma is linked with a potential fluctuation through the adiabatic response. The adiabatic response is simply a parallel force balance between the pressure force and the electrostatic force. A simplified version of Eq. 3.3 can be written:

$$\nabla_{\parallel} p_e = en \nabla_{\parallel} \phi + R v_{\parallel e}, \quad (5.1)$$

where the term $R v_{\parallel e}$ represents effects such as electron inertia, resistivity, and electromagnetic induction. If $R = 0$, the electrons are said to be adiabatic, meaning $\nabla_{\parallel} p_e = en \nabla_{\parallel} \phi$. When T_e fluctuations are neglected and $\nabla_{\parallel} \neq 0$, this integrates to the Boltzmann expression:

$$n = n_0 e^{e\phi/T_e}. \quad (5.2)$$

For any R and T_e fluctuations, the parallel electron dynamics couple the pressure to the potential as long as the parallel wavelength k_{\parallel} is finite. The perpendicular electric field associated with the potential fluctuation has a component in the azimuthal direction with $k_{\perp} \gg k_{\parallel}$. This creates a radial $\mathbf{E} \times \mathbf{B}$ drift that advects the pressure in the radial direction. Because of the radial pressure gradient, the fluctuation propagates azimuthally as a wave at the drift speed $v_{De} = \frac{T_e}{eB} \frac{\partial \ln N_0}{\partial r}$ [Che06] in the electron diamagnetic drift direction. If there is a small phase difference between the pressure and the potential of the wave (the result of $R \neq 0$), the equilibrium pressure gradient will enhance the fluctuation, causing instability. Since $p_e = n_e T_e$, the pressure fluctuation may be due to either a density fluctuation, an electron temperature fluctuation, or both. The universal instability generally refers to the situation where an equilibrium density gradient drives a density fluctuating wave. But a temperature gradient driving a temperature fluctuation wave is also possible, and may be called a thermal drift wave [MTK11]. It's not necessary, however, to separate them, and I will just refer to both of these as drift waves.

The LAPD equation set (Eqs. 4.1-4.4) supports such drift waves, which are unstable with the parameters and profiles used in the simulations. The growth rate as a function of the azimuthal wavenumber m is shown in Fig. 5.1 a) for the LAPD parameters in Table 4.3 and profiles in Fig. 4.2. The growth rates are found by simulating the linearized version of Eqs. 4.1-4.4 in BOUT++ with the three different simple axial boundary conditions: periodic, zero-value (Dirichlet), and zero-derivative (Neumann). The linear equations simply omit the advective nonlinearities and the source terms, though the source terms have no effect on any of the linear modes besides $m = 0$ modes. The simulations are run for long enough so that the fastest growing modes can dominate the dynamics.

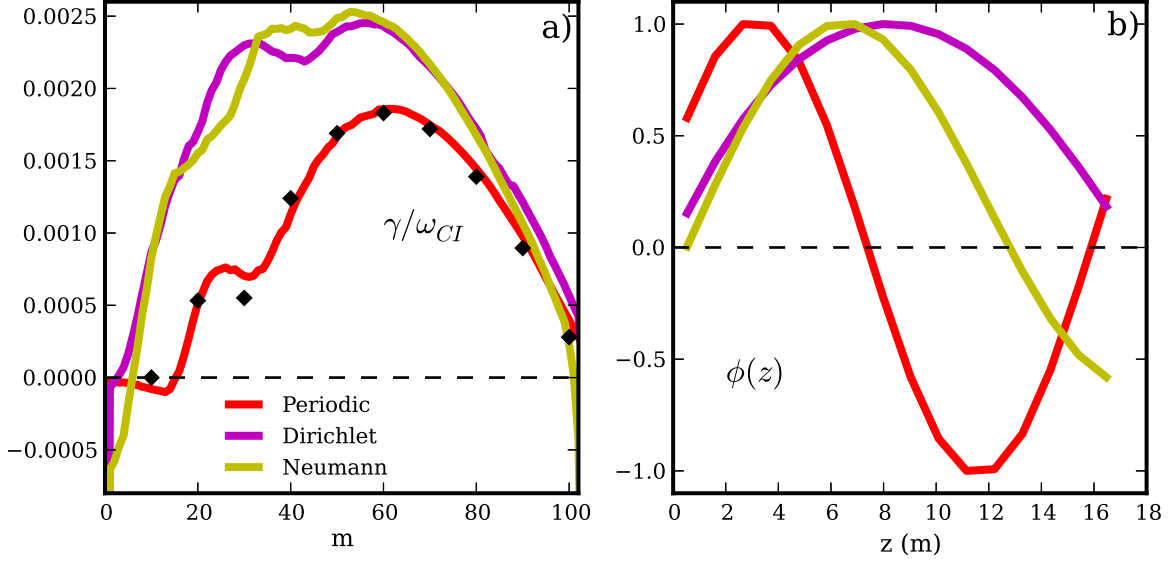


Figure 5.1: Linear drift wave a) growth rates and b) axial structures

The solid curves in Fig. 5.1 are calculated from the simulation results using the formula, $\gamma_m = \frac{\partial E_m}{\partial t} / (2E_m)$ where E_m is the energy of the fastest growing linear eigenmode with azimuthal mode number m . The energy is defined in Chapter 6. The details of obtaining γ_m are explained in that chapter, but for now, it is sufficient to state that this procedure calculates γ_m at a particular time using only the structures of the fluctuating quantities: N , ϕ , $v_{\parallel e}$, and T_e . An alternative way to calculate γ_m is to use BOUT++'s Fourier filtering capabilities and run many simulations where each one filters out a different azimuthal mode. Then, I take the log of the envelope of one or several of the fluctuating quantities and calculate the slope of the line, which gives the growth rate for each particular simulation. This procedure uses the time signal of the fluctuations rather than their spatial structure to calculate the growth rate, thus providing a check on the first method. The results using this alternative method for the periodic case are shown with the black diamonds in Fig. 5.1 a), which agree well with the curve calculated using the alternative energetic structure-based calculation. I do this

check with all of the simulations to ensure consistency. This second method is more time consuming, so I only sample a few values of m . Furthermore, it's difficult to get growth rates when $\gamma_m < 0$ using this second method.

The difference in the growth rate curves with the different boundary conditions is due to the different $k_{\parallel} = \frac{2\pi n}{L_{\parallel}}$ where n is the axial mode number. The periodic simulation restricts n to integer values, while the Dirichlet and Neumann simulations allow for any fractional n . The largest growth rate occurs for $n \sim 1/2$. The Dirichlet and Neumann axial structures for the most unstable m mode, shown in Fig. 5.1 b), reflect this. The periodic simulation, which has $n = 1$ structure, has a smaller growth rate, especially at low m . Note that in Fig. 5.1 b), the axial boundaries are not plotted. For instance, the zero-valued boundaries for the Dirichlet simulation are not shown. Also, the axial structures are taken at one random point in the $r - \theta$ plane and at one time point, and are normalized to their maximum value.

5.1.2 Conducting Wall Mode

I now consider the linear instability that can exist in a plasma bounded by two conducting walls on the boundaries where the magnetic field lines terminate (the axial boundaries) [BRT91, BCR93, XRD93]. The instability is actually of the drift wave variety, but unlike the drift waves discussed above, the pressure-potential coupling mechanism is through the sheath boundary response rather than through the adiabatic response. The Bohm sheath boundary conditions that were derived in Sec. 4.2.2 can provide this coupling. As already noted, these boundary conditions are not necessarily the correct ones for LAPD, but are somewhat idealized. Yet, it is still academically instructive to apply such an idealized boundary condition to LAPD because it creates this new linear instability, which can be used to test the robustness of LAPD's nonlinear instability.

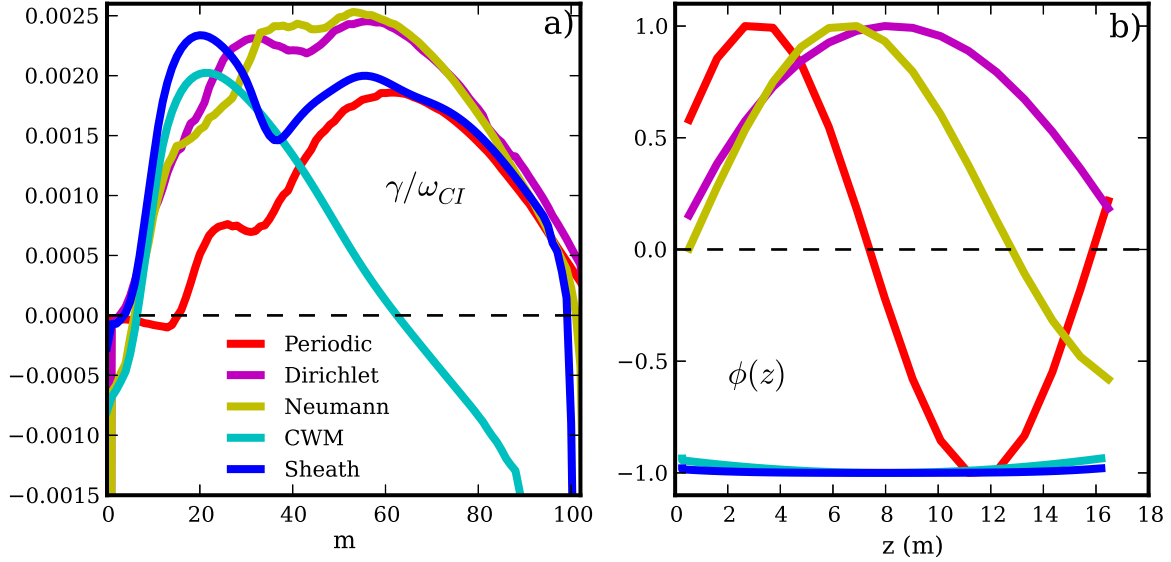


Figure 5.2: Linear conducting wall mode a) growth rates and b) axial structures

The conducting wall mode (CWM) instability in the case considered here is purely an electron temperature gradient instability, although other types of gradients can cause it [BCR93]. Electron temperature fluctuations are advected by electrostatic potential fluctuations and feed off the equilibrium electron temperature gradient as in the case of the thermal drift waves. However, in contrast to the thermal drift waves, the coupling between the temperature and potential fluctuations comes through the sheath boundary condition rather than through the adiabatic response. Furthermore, the CWM can have (nearly) $k_{\parallel} = 0$ flute-like behavior. The coupling mechanism is as follows: an electron temperature perturbation – say a positive constant fluctuation along a small flux tube – increases the sound speed and the electron thermal speed on the flux tube. Since the ions must enter the Bohm sheath at the sound speed by being accelerated by a parallel electric field, the temperature increase must coincide with an increase in the parallel potential gradient as derived in Eq. 4.10. Additionally, the increased electron thermal speed causes an increase in the floating potential along the flux

tube. These serve to couple the electron temperature to the potential.

The CWM can be isolated from the normal drift waves by removing the adiabatic response from the full LAPD equation set, and of course using the Bohm sheath boundary condition of Eq. 4.10. Removal of the adiabatic response in this case means removal of the $\nabla_{\parallel} p_e$ and the $0.71 \nabla_{\parallel} T_e$ terms in the parallel momentum equation (Eq. 4.2). This causes the density fluctuation N to become a passive scalar, so Eq. 4.1 can be removed as well with no consequence. So the isolated linear CWM equations are:

$$\partial_t v_{\parallel e} = \frac{m_i}{m_e} \nabla_{\parallel} \phi - \nu_e v_{\parallel e}, \quad (5.3)$$

$$\partial_t \varpi = -N_0 \nabla_{\parallel} v_{\parallel e} - \nu_{in} \varpi + \mu_{\phi} \nabla_{\perp}^2 \varpi, \quad (5.4)$$

$$\partial_t T_e = -\mathbf{v}_E \cdot \nabla T_{e0} + \frac{2}{3N_0} \kappa_{\parallel e} \nabla_{\parallel}^2 T_e - \frac{2m_e}{m_i} \nu_e T_e + \mu_T \nabla_{\perp}^2 T_e, \quad (5.5)$$

The CWM growth rate curve is shown in Fig. 5.2 a). The CWM is most unstable at values of $m \sim 20$, which is much lower than the $m \sim 60$ values of the drift waves. Furthermore, the CWM maximum growth rate is about equal to the drift wave growth rates. And from Fig. 5.2 b), the CWM axial structure is flute-like ($k_{\parallel} \simeq 0$). Finally, the growth rate curve of the full set of equations along with the sheath boundary condition is shown in this figure as the curve labeled “sheath.” This set of equations contains the drift wave and CWM instabilities. From both Figs. 5.2 a) and b), it is clear that the sheath simulation is dominated by the CWM at $m \leq 20$, which in fact is where the growth rate is maximum. At $m \geq 40$, the drift waves dominate.

5.2 LAPD Turbulence: A Visual Examination

When I simulate the full LAPD equation set with the advective nonlinearities and source terms, I find that the simulation develops into a turbulent state. To

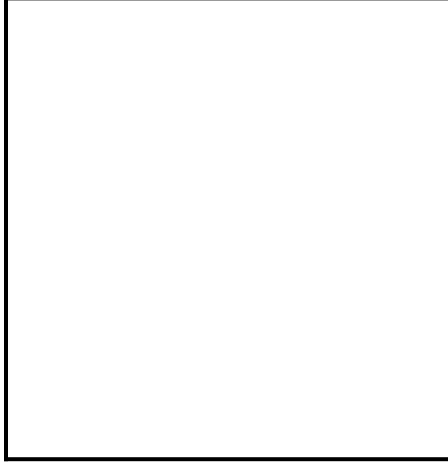


Figure 5.3: 3D turbulent simulation animation

start the simulation, I initialize each fluctuation quantity (N , ϕ , $v_{\parallel e}$, and T_e) with a small random 3D spatial structure. The structure evolves and a coherent structure emerges (the fastest growing linear eigenvector), which grows exponentially in time. Once the normalized fluctuations reach values on the order of $0.01-0.1$, they saturate and appear to be turbulent. A 3D animation of the density fluctuation N is shown in Fig. 5.3. The animation shows a $1/8$ th wedge of the simulated annulus to make the axial extent of the annulus visible. The animation begins right before the fastest growing mode structure becomes dominant. The fastest growing mode dominates the structure for some time, where there is a clear coherent wave structure that simply propagates in the electron diamagnetic drift direction. This stage is called the linear stage since the linear terms in the equations dominate the evolution. Note that the axial structure in the linear stage has a finite wavelength about half of the length of the animation domain. The axial boundary conditions used here (Neumann) allow for such a structure.

Soon, the coherent eigenmode structure, which has been growing in magnitude, saturates and transitions to a turbulent-looking state that I call the turbulent

stage. The evolution of the RMS fluctuation amplitude of the density and potential is shown in Fig. 5.4 a). The potential is separated into a flux-surface-averaged component ϕ_{fs} and the remainder $\phi - \phi_{fs}$. ϕ_{fs} quantifies the amplitude in the zonal flow, which appears in Fig. 5.4 a) to possibly have some role in the initial saturation, but has a relatively small magnitude in the turbulent stage. For all the fluctuations, the exponential growth period during the linear stage is followed by saturation corresponding to the visual change from coherent to turbulent spatial structures in the animation. Upon transition to the turbulent stage, I notice in the animation that there is also a qualitative change in the axial mode structure. The axial structures elongate, looking more flute-like than in the linear stage. I confirm this by taking the axial Fourier transform of the density fluctuations and plotting the RMS values of the different axial mode numbers in Fig. 5.4 b). The linear stage is dominated by the $n = 1$ Fourier component, while the turbulent stage is dominated by the $n = 0$ flute mode component. I found this to be an interesting and unexpected transition when I first identified it. There is not only the expected bifurcation from linear waves to turbulence, but also the unexpected bifurcation from linear drift wave structures to turbulent flute-like structures. I will discuss why this is unexpected in the upcoming chapters, and I will show in detail what causes it. But take note that this is a key finding. This $n = 0$ dominance in the turbulent stage is the main subject of the remaining chapters.

However, before I jump into the analysis of the $n = 0$ mode dominance, I continue to look at simple and common turbulence analysis techniques to describe the nature of the turbulence and to validate the simulations. Continuing on with the visual examination, I show one visual comparison between the simulation and experiment. For the experimental visual, I use a processed fast camera movie. The camera records the light intensity given off by the plasma. The light is primarily due to line radiation of the helium atoms and ions. It should be some function of plasma density, neutral density, and plasma temperature. Noting that the

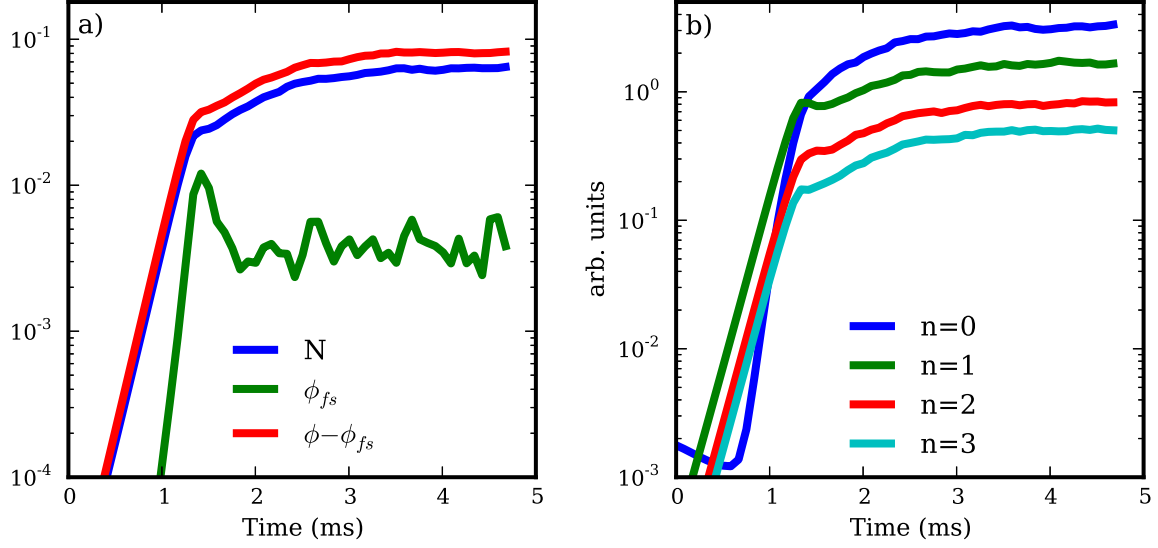


Figure 5.4: RMS time evolution of a) fluctuations and b) axial mode numbers

comparison is certainly not exact, I show the experimental camera data next to corresponding simulation data of the density N signal during the turbulent stage. This is shown in Fig. 5.5. The animations cover the same spatial domain and last for equal time intervals (about 2 ms). Both are simply fluctuation data with the time-independent background not included (subtracted out from the camera data).

Visual comparisons like this are certainly not quantitative, and at best this comparison reveals that both simulation and experiment appear turbulent and contain similarly sized spatial structures and similar time scales. The camera data can be a valuable tool since it provides so much simultaneous spatial data – something that is difficult to do with probes. Nevertheless, I do not proceed here with detailed statistical analysis of the camera data or any quantitative comparisons between the camera and simulation. This work is left for future studies. Rather, I now focus on statistical analysis of the simulation data, and compare it to experimental Langmuir probe data when possible.

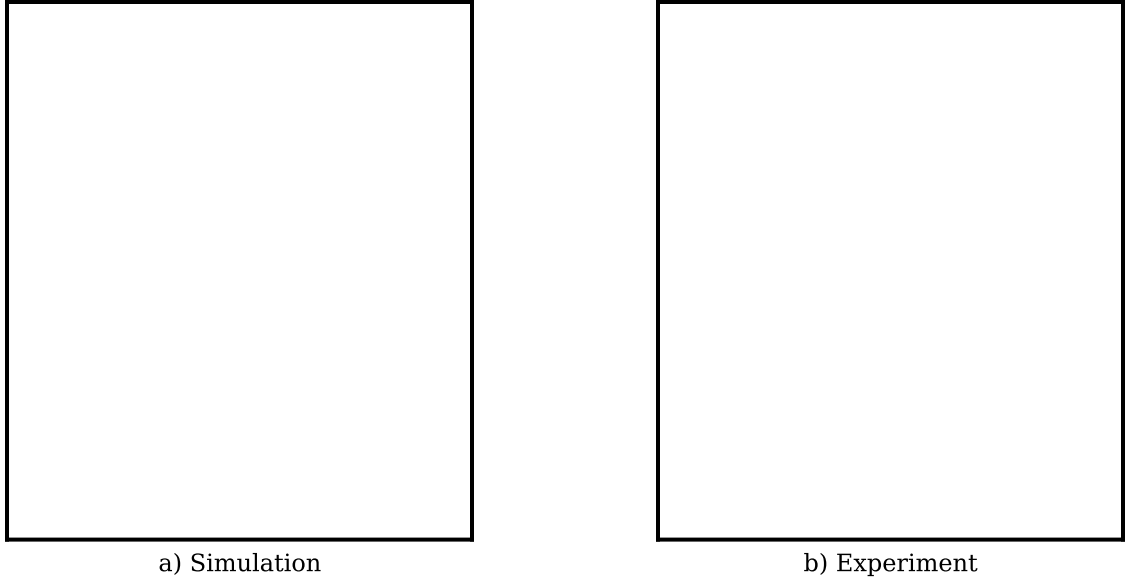


Figure 5.5: Turbulent movies

5.3 LAPD Turbulence: A Statistical Examination

Turbulent or chaotic systems do not produce realistically predictable end states. It's therefore useful to look at time series and spatial states of such systems in a statistical way. Simulations and experiment can produce such data and be compared, which is the best way to validate simulations. Furthermore, turbulent plasma systems are often characterized by statistical properties such as shapes and magnitudes of spectra, pdfs, and spatial and temporal correlations.

There are many different kinds of experimental measurements, but I focus here only on Langmuir probe measurements. The Langmuir probes in LAPD generally provide time series data although I do have some two-probe data that provides certain spatial information. Langmuir probes do not directly measure any of the independent state or flux variables of the simulation ($N, \phi, v_{\parallel e}, T_e$), but these quantities can be derived from the measurements. The probes are biased to a known potential (with respect to a reference like the cathode potential), and

the current they draw from the plasma is measured. As long as the probes are biased sufficiently below the plasma potential so as to repel most electrons, they develop sheaths around them in the same way as the conducting plates considered in Sec. 4.2.2. The ion current to the probe is [Hut02]

$$I_i \sim \frac{1}{2} e A_s n c_s \quad (5.6)$$

where A_s is the sheath area, approximately equal to the probe area, and the factor of $\frac{1}{2}n$ is the reduction of density at the sheath edge compared to the main plasma. The probe may be biased negatively enough so that all electrons are repelled. The current collected is just that of Eq. 5.6, called the ion saturation current. As the probe voltage is swept positively from this point, more electrons are collected. The total current to the probe then takes the form [Hut02]

$$I = e A_s n c_s \left[\frac{1}{2} - \left(\frac{m_i}{2\pi m_e} \right)^{1/2} e^{eV_p/T_e} \right], \quad (5.7)$$

where V_p (which is negative) is the potential of the probe with respect to the plasma potential. When $I = 0$, the probe potential is at the floating potential: $\frac{eV_f}{T_e} = \frac{1}{2} \ln \left(\frac{\pi m_e}{2m_i} \right)$. This relation isn't used to obtain the temperature because the plasma potential isn't known, meaning V_f isn't either. The temperature, however, can be obtained by sweeping the probe potential to get $\frac{\partial I}{\partial V_p}$, which is an exponential function of V_p . So the \ln of this function produces a straight line. Then, the temperature is:

$$T_e = e(I - I_i) / \frac{\partial I}{\partial V_p}. \quad (5.8)$$

Once the temperature is found, which gives the value for the sound speed, the ion saturation current can be used to obtain the density. Furthermore, knowledge of the temperature and the floating potential gives the plasma potential: $\phi =$

$V_f - \frac{T_e}{2e} \ln \left(\frac{\pi m_e}{2m_i} \right)$. The plasma potential may alternatively be identified as the value of the potential on the probe at which the electron current saturates because no sheath develops when the probe potential equals the plasma potential. Thus, swept Langmuir probe data processed under these theoretical calculations can give values for N , ϕ , and T_e that can be compared to the corresponding simulation variables.

A comparison of statistical properties of the experimental and simulation density fluctuations is shown in Fig. 5.6. I show results from five different simulations that all use the full nonlinear LAPD equation set (Eqs. 4.1-4.4) but differ in the axial boundary conditions as follows: 1) Periodic – uses periodic axial boundary conditions. 2) Sheath – uses Bohm sheath boundary conditions in Eq. 4.10. 3) $n = 0$ suppressed – uses axial boundary conditions, however, the axial average (k_{\parallel} or $n = 0$) density and temperature fluctuation components are artificially removed from the simulation. 4) Dirichlet – uses zero-value axial boundary conditions. 5) Neumann – uses zero-first-derivative axial boundary conditions. I will discuss the $n = 0$ suppressed simulation more in Chapter 7, but for now it is sufficient to say that this simulation does not contain the nonlinear instability and is thus a control case by which to compare the others. It still contains the same linear instabilities as the Periodic simulation, however.

Fig. 5.6 a) shows the frequency power spectrum of the density fluctuations. I use a sliding Hamming window on the time series data and take the FFT, then take a volume average from 15 to 35 cm to get each simulation curve. I use the same technique for the experimental density fluctuation data, except I only have probe data at one location in the $\theta - z$ plane. The axial location is near the center of the machine. Fig. 5.6 b) shows the probability distribution function (PDF) of the density fluctuations, while Fig. 5.6 c) shows the RMS amplitude of the density fluctuations as a function of radius. Fig. 5.6 d) plots the radial k_r power spectrum of the simulations. I don't have experimental radial spectra data, which requires

multiple probes at different radii. Fig. 5.6 e) is the azimuthal m_θ power spectra. Two probes separated azimuthally are used to obtain the experimental spectra. Finally Fig. 5.6 f) is the axial k_\parallel spectra, and I don't have experimental axial spectra due to the difficulty of aligning two probes along a field line a significant distance from each other, which is required because of the long axial wavelengths of the modes.

Fig. 5.6 contains a lot of information about the simulations and experiment. The first obvious result is that the $n = 0$ suppressed simulation is statistically much different than all of the other simulations and the experiment. The density fluctuations of this simulation are a factor of 2-3 lower than that of the other simulations and the experiment. Furthermore, this simulation has peaks in the frequency, m_θ , and k_\parallel spectra that are unique and apparently inconsistent with the experiment. Its spatial spectra peak at $m_\theta \sim 30$ and $k_\parallel \rho_s \sim 0.002 \rightarrow n = 1$, which is somewhat consistent with the linear growth rate spectra of Fig. 5.1, although the m_θ peak location is somewhat less than the maximum linear growth rate value of m_θ , which is around 60 when the axial boundaries are periodic. This differs significantly from all of the other simulations which have peaks at $m_\theta \sim 10$ (if they peak at all) and $k_\parallel \rho_s = 0$. Again, as was clear from Fig. 5.4 b), all of the other simulations are strongly dominated by $n = 0$ axial mode numbers, which will be explained in the upcoming chapters as due to the nonlinear instability.

Moreover, all of the simulations other than the $n = 0$ suppressed one have qualitatively and semi-quantitatively similar statistical properties. I note that on a quantitative level, the Dirichlet and Neumann simulations have fluctuation levels about 1.5 times less than the Periodic and Sheath simulations. I don't fully understand the reason for this, but note that the axial wavenumber spectra in Fig. 5.6 f) are shallower for the Dirichlet and Neumann simulations. This certainly affects the energy injection and energy dissipation, as will be seen in the following chapters. Nevertheless, I don't claim that the Dirichlet and Neumann

simulations are less consistent with the experiment than the Periodic and Sheath simulations because of the relatively inconsistent fluctuation amplitude of the former simulations. The reason is that I have a free parameter, namely the artificial diffusion coefficient, which affects the overall fluctuation level without significantly affecting the shapes of the spectra. I tuned this parameter to be 1.25×10^{-3} (see Chapter 4) to match the fluctuation level of the Periodic simulation with experiment. Had I tuned this parameter with the Dirichlet or Neumann simulations in mind, it would seem that the Periodic and Sheath simulations had fluctuation levels too large. So, in fact, all four of these simulations are qualitatively consistent with the experiment, and they are also quantitatively consistent with the caveat that the quantitative match is caused by tuning a single free parameter. I don't provide any error analysis to quantify the agreement between simulation and experiment, but rather just use an eye test. The fact that several different statistical properties agree between simulation and experiment lends evidence to our claim that the simulation model is relatively well validated.

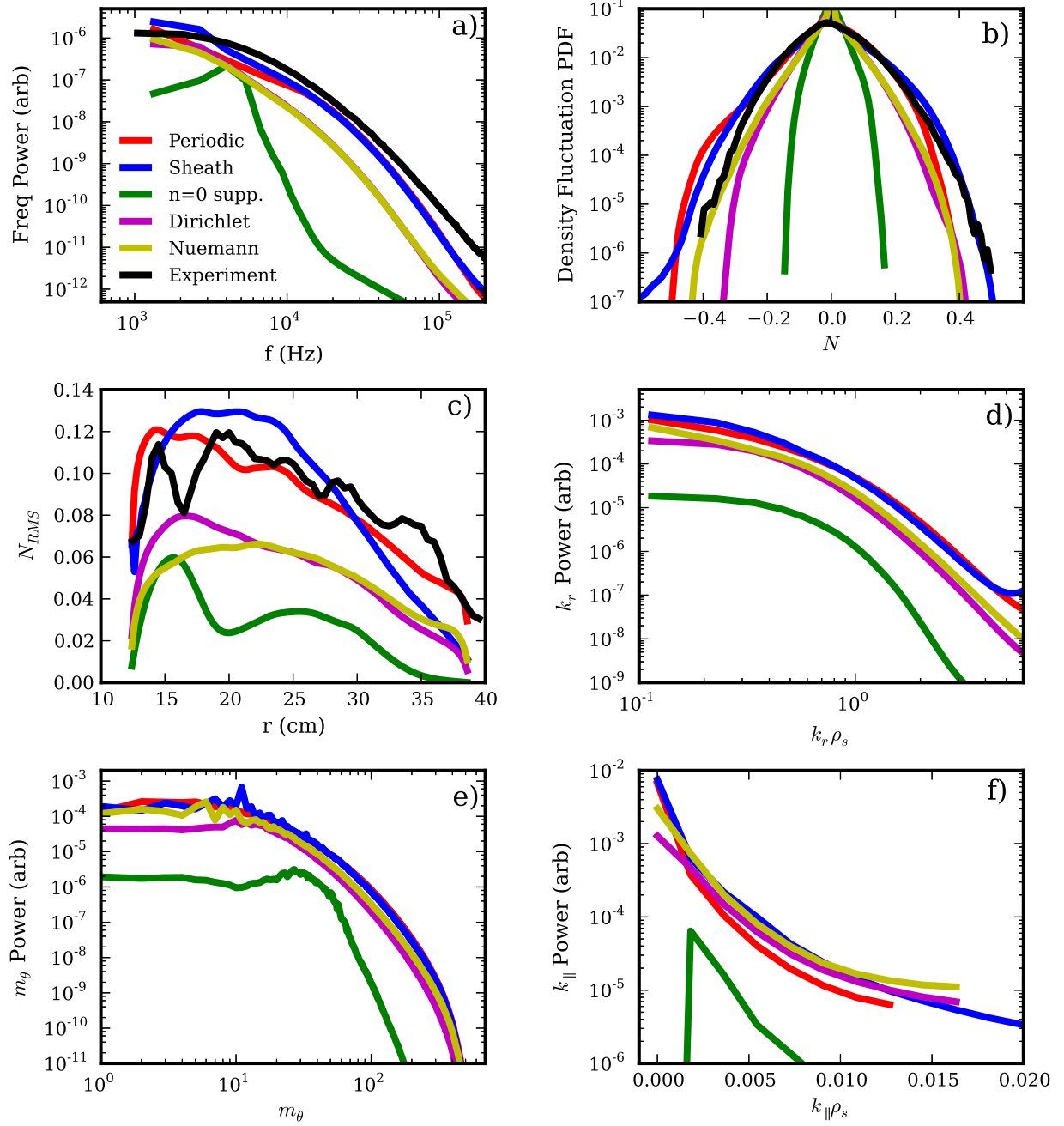


Figure 5.6: Density statistics

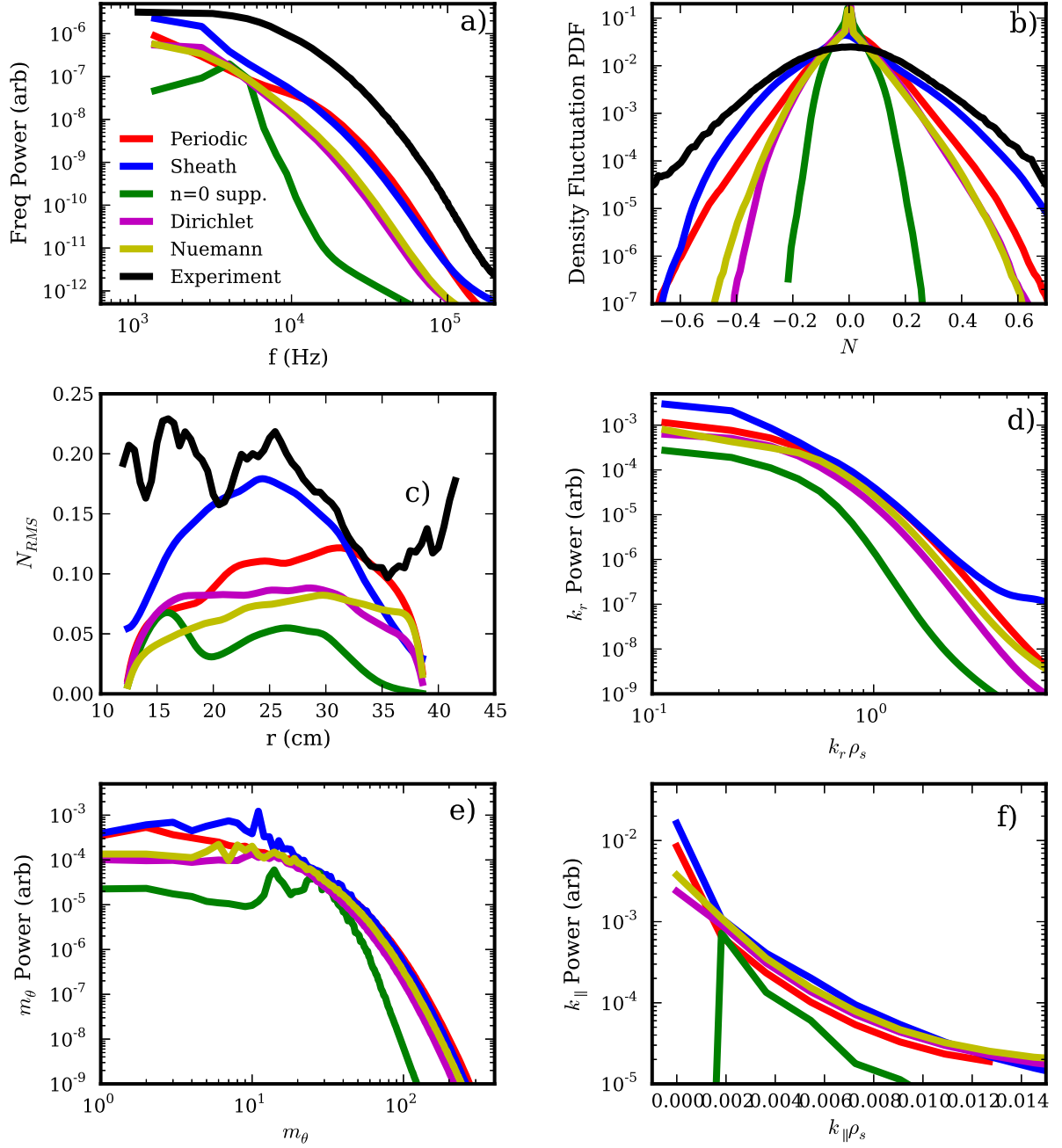


Figure 5.7: Potential statistics

CHAPTER 6

Energy Dynamics Formalism

6.1 Total Energy and Dynamics

6.2 Spectral Energy Dynamics

CHAPTER 7

Nonlinear Instability for the Periodic Simulation

7.1 The Energy Spectra

7.2 Energy Dynamics Result

7.3 $n=0$ Suppression

CHAPTER 8

Energy Dynamics for the Non-periodic Simulations

- 8.1 The Importance of Axial Boundary Conditions
- 8.2 Fourier Decomposing Non-periodic Functions
- 8.3 Energy Dynamics Results
- 8.4 Linear vs Nonlinear Structure Correlation

CHAPTER 9

Finite Mean Flow Simulations

9.1 The LAPD Biasing Experiment

9.2 New Linear Instabilities

9.3 Statistical Comparisons to Experiment

9.4 Energy Dynamics Results

CHAPTER 10

Conclusion

APPENDIX A

The BOUT++ Code

A.1 The Object-Oriented Fluid Framework

A.2 Explicit Finite Differences

A.3 The Physics Inputs

APPENDIX B

Grid Convergence

REFERENCES

- [Ara66] A. Arakawa. “Computational Design for Long-Term Numerical Integration of the Equations of Fluid Motion.” *J. Computational Physics*, **1**:119–143, 1966.
- [BCR93] H. L. Berk, R. H. Cohen, D. D. Ryutov, Yu. A. Tsidulko, and X. Q. Xu. “Electron temperature gradient induced instability induced in tokamak scrape-off layers.” *Nuclear Fusion*, **33**:263, 1993.
- [Bra65] S. I. Braginskii. “Transport processes in a plasma.” In M A Leontovich, editor, *Reviews of Plasma Physics*, volume 1, pp. 205–311. Consultants Bureau, New York, 1965.
- [BRT91] H. L. Berk, D. D. Ryutov, and Yu. A. Tsidulko. “Temperature-gradient instability induced by conducting end walls.” *Phys. Fluids B*, **3**:1346, 1991.
- [Che06] F. F. Chen. *Introduction to Plasma Physics and Controlled Fusion*. Springer, 2006.
- [DUX09] B. D. Dudson, M. V. Umansky, X. Q. Xu, P. B. Snyder, and H. R. Wilson. “BOUT++: A framework for parallel plasma fluid simulations.” *Computer Physics Communications*, pp. 1467–1480, 2009.
- [Hut02] I. H. Hutchinson. *Principles of Plasma Diagnostics*. Cambridge University Press, 2002.
- [HW83] A. Hasegawa and M. Wakatani. “Plasma Edge Turbulence.” *Phys. Rev. Lett.*, **50**:682–686, 1983.
- [LRH12] J. Loizu, P. Ricci, F. Halpern, and S. Jolliet. “Boundary conditions for plasma fluid models at the magnetic presheath entrance.” *Phys. Plasmas*, **13**:122307, 2012.
- [MTK11] K. D. Makwana, P. W. Terry, J. H. Kim, and D. R. Hatch. “Damped eigenmode saturation in plasma fluid turbulence.” *Phys. Plasmas*, **18**:012302, 2011.
- [PUC10a] P. Popovich, M. V. Umansky, T. A. Carter, and B. Friedman. “Analysis of plasma instabilities and verification of BOUT code for linear plasma device.” *Phys. Plasmas*, **17**:102107, 2010.
- [PUC10b] P. Popovich, M. V. Umansky, T. A. Carter, and B. Friedman. “Modeling of plasma turbulence and transport in the Large Plasma Device.” *Phys. Plasmas*, **17**:122312, 2010.

- [RR10] B. Rogers and P. Ricci. “Low-frequency turbulence in a linear magnetized plasma.” *Phys. Rev. Lett.*, **104**:225002, 2010.
- [SC03] A. N. Simakov and P. J. Catto. “Drift-ordered fluid equations for field-aligned modes in low- β collisional plasma with equilibrium pressure pedestals.” *Phys. Plasmas*, **10**:4744, 2003.
- [SCR12] D. A. Schaffner, T. A. Carter, G. D. Rossi, D. S. Guice, J. E. Maggs, S. Vincena, and B. Friedman. “Modification of Turbulent Transport with Continuous Variation of Flow Shear in the Large Plasma Device.” *Phys. Rev. Lett.*, **109**:135002, 2012.
- [Sta00] P. C. Stangeby. *The plasma boundary of magnetic fusion devices*. Institute of Physics Publishing, 2000.
- [Wes04] J. Wesson. *Tokamaks*. Clarendon Press, 2004.
- [XRD93] X. Q. Xu, M. N. Rosenbluth, and P. H. Diamond. “Electron-temperature-gradient-driven instability in tokamak boundary plasma.” *Phys. Fluids B*, **5**:2206, 1993.